RESEARCH ARTICLE



Flame image velocimetry: seedless characterization of post-reflected-shock velocities in a shock-tube

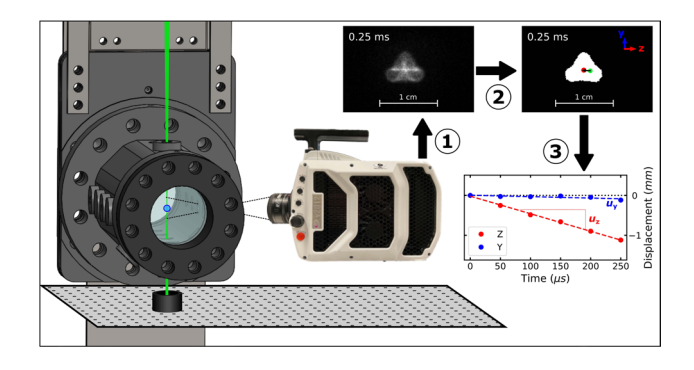
Adam J. Susa¹ · Ronald K. Hanson¹

Received: 15 September 2021 / Revised: 7 December 2021 / Accepted: 11 January 2022 / Published online: 28 January 2022 © The Author(s), under exclusive licence to Springer-Verlag GmbH Germany, part of Springer Nature 2022

Abstract

The use of a laser-ignited expanding flame as a virtual particle for seedless velocimetry of a flammable mixture is described and demonstrated, a method referred to as flame image velocimetry. Within an expanding flame, the burned gas is nominally stagnant relative to the local flow field, such that the motion of the flame centroid can be interpreted as an advected particle and serve as the basis of a single-point velocity measurement. This technique is applied to study the post-reflected-shock (region-5) environment in a shock tube using propane and n-heptane as fuels, lean equivalence ratios $(0.3 \le \phi \le 0.9)$, and oxidizers consisting of 18.1% to 21.4% O_2 balanced with combinations of nitrogen, argon, and helium diluents; thermodynamic conditions spanned the temperature and pressure ranges 571 K $\le T_5 \le 1076$ K and 1.0 atm $\le P_5 \le 1.9$ atm. A novel imaging configuration is devised to provide simultaneous, dual-perspective, high-speed images of expanding flames ignited 10.3 cm from the end wall of a shock tube. From the resulting images, the three-dimensional velocity field of the region-5 core gas is measured, revealing near-zero velocities in the radial directions and small, but measurable, velocities along the axis of the shock tube. Two conceptual models for axial region-5 velocity are developed: residual velocity resulting from the attenuation of the incident and reflected shock waves and pressure-change-induced velocity associated with temporal variations in the post-reflected-shock pressure. While neither model alone is predictive of the measured axial velocities, their combination systematically recovers the measured results, suggesting that these two conceptual models, based on experimentally measured pressures, are sufficient to predict the region-5 velocity in shock-tube experiments.

Graphical Abstract



Adam J. Susa asusa@stanford.edu

Ronald K. Hanson rkhanson@stanford.edu

1 Introduction

In studies of high-temperature gas-phase chemistry, the shock tube serves as the pre-eminent apparatus for zero-dimensional kinetic studies, readily producing post-reflected-shock (region-5) temperatures in the range $400 \, \mathrm{K} < T_5 < 10,000 + \mathrm{K}$ and pressures (P_5) from sub-atmospheric to 100s of atmospheres on microsecond time



Mechanical Engineering, Stanford University, 452 Escondido Mall, Stanford, CA 94305, USA

scales (e.g., Shepherd 1948; Bauer 1963; Tsang and Lifshitz 1990; Hanson and Davidson 2014). This ability to nearly instantaneously change the thermodynamic state of a gaseous mixtures enables the study of even the fastest kinetic processes, including high-temperature combustion chemistry and the vibrational relaxation of air at hypersonic-relevant conditions.

In an ideal shock tube, the reflected shock wave perfectly stagnates the test gas in region-5 (Gaydon and Hurle 1963); the corresponding assumption of "quiescent" or "stagnant" region-5 gas is found throughout the shock-tube literature (e.g., Huang et al. 2004; Davidson et al. 2010; Ninnemann et al. 2018; Camm et al. 2018). As the driven-side end wall of the shock tube represents an impermeable boundary, stagnation of the gas at the end wall is expected to hold exactly even under real-world shock-tube conditions and is foundational to solution methods for the shock-jump equations (e.g., Emanuel 2000; Campbell et al. 2017). However, in real facilities, quiescence is expected to break down away from the end wall due to non-ideal effects of the end-wall thermal and side-wall boundary layers (Mark 1958).

The flow field associated with a shock-boundary-layer interaction (SBLI) has been the subject of extensive theoretical (e.g., Davies and Wilson 1969), experimental (e.g., Kleine et al. 1992; Yoo et al. 2010; Yamashita et al. 2012), and numerical investigation (e.g., Weber et al. 1995; Grogan and Ihme 2017). Nevertheless, few studies report the corresponding impact of the boundary layer on the core-gas flow field. To the authors' knowledge, the baseline particle image velocimetry (PIV) experiments of Wagner et al. (2015, 2018) in a multi-phase shock tube are the only direct post-reflected-shock gas velocity measurements reported in the literature. Performed in a square test section located one meter from the driven-side end wall, the PIV measurements show counter-flowing gases in region-5, with the core gas retaining velocity toward the end wall after passing through the reflected shock and the flow in the boundary layer reversing to flow away from the end wall. While the one-meter measurement location is not immediately relevant to kinetics studies typically performed two centimeters or nearer to the end wall, the velocities measured to be on the order of 10's of meters per second nonetheless raise questions regarding the degree to which region-5 quiescence may also break down at more relevant axial conditions.

Details of the region-5 flow field are especially pertinent to the shock-tube flame speed method. In this approach to measuring premixed laminar flame speeds, first introduced by Ferris et al. (2019), a shock tube is used as an impulse heater for the unburned-gas. Flames are ignited behind the reflected shock using a plasma spark generated through laser-induced breakdown (LIB). LIB serves as a relatively non-intrusive alternative to the use of electric sparks as are commonly employed in static flame vessels, as the requisite

protruding electrodes would disturb the high-speed, post-incident-shock (region-2) flow. Propagation of the resulting expanding flame is recorded using high-speed imaging, allowing for extraction of the laminar flame speed. This method has been demonstrated to enable experiments at unburned-gas temperatures that would not otherwise be accessible to flame-speed measurements, but are relevant to practical engine applications (e.g., Susa et al. 2019, 2021). Nevertheless, the interpretation of such measurements has required assumptions regarding the flow field in which flames are ignited, such that characterization of the three-dimensional (3-D) core-gas velocity in a shock tube could provide beneficial new insights toward enhancing the fidelity of such experiments.

2 Flame image velocimetry method

The validity of tracer-based velocimetry methods is dependent upon the extent to which the particles accurately follow the underlying flow field. When applied to gaseous flows, PIV methods typically require micron-scale solid particles or aerosol droplets (Melling 1997). While compatible tracers and seeding techniques exist for even harsh, high-temperature, and reactive environments (e.g., Willert et al. 2007), seedless diagnostics are nonetheless required to enable measurements in certain applications, such as within high-purity shock tubes where tracer particles might otherwise contaminate the facility.

Flame image velocimetry (FIV) is proposed here as a seedless, single-point velocity measurement technique that can be readily implemented in flow systems compatible with flammable gas mixtures and combustion events. Unlike traditional PIV, which relies on tracking physical particles or droplets, FIV instead tracks the bulk translation of a premixed flame as it is carried by the underlying flow field. Under quiescent conditions, a freely propagating expanding flame remains nominally stationary. However, if a bulk velocity field exists in the unburned gas, the flow fields are superimposed, with the burned gas taking on the velocity of the underlying flow field. In this manner, the centroid of the flame tracks the average bulk velocity of the unburned gas and can be treated as a "virtual particle" with which the underlying flow-field velocity can be measured. While buoyancy effects can become relevant to expanding flames exhibiting low flame speeds at relatively long time scales (Berger et al. 2020), the effect of buoyancy is negligible at the short measurement times considered in the present FIV measurements.

This behavior of flames being advected by bulk flows has been documented in various forms through previous studies; a few relevant examples are introduced here in brief. Jones et al. (1998) studied turbulent flame propagation behind



reflected shocks in a shock tube with an upstream grid to introduce turbulence into the flow. In that study, the authors reported an equipment failure that undermined an effort to measure the mean flow velocity using laser doppler anemometry (LDA), and the researchers did not make use of the observed bulk motion of the flame to measure the velocity. Beduneau et al. (2009) performed velocity compensation in their study of laser ignition in a laminar flow; this correction was premised on the fact that the flame was carried by the flow field, but made use of the known flow velocity rather than the observed translational velocity of the flame. Kobayashi et al. (2019) measured differences in the propagation speed of the top and bottom of a flame kernel that resulted from buoyancy under normal gravity, but the analysis did not continue to the point of extracting a corresponding bulk velocity of the flames. Most recently, Jo and Gore (2022) measured flame kernel velocities in their study of hydrogen ignition by LIB in jet, showing the kernel velocity came to match the known jet velocity after a response time of about $20 \mu s$.

The FIV technique is related to the laser-induced plasma image velocity (LIPIV) method introduced by Shi et al. (2019). Like LIPIV, the present realization of FIV uses a laser-induced plasma to non-intrusively introduce a virtual particle into a flow. The primary difference between the LIPIV and FIV methods lies in the source of emission imaged following the laser-induced breakdown (LIB). In LIPIV, only emission from the plasma itself is present, which exhibits a short radiative lifetime and limits the maximum inter-frame measurement time. Shi et al. (2019) reported interframe times of 50-100 µs as typical in their study, requiring camera exposure times of 20–100 µs to acquire sufficient signal. In the FIV method, a sustained flame is ignited, providing persistent chemiluminescence that can be imaged over much longer timescales (frames recorded over a span of 250 µs were used in this study), thus providing greater sensitivity to small flow velocities. Additionally, as the flame emission does not decay in time, short exposure times (10 µs or less) can be used independent of the interframe time, thus reducing potential impacts from motioninduced blurring in the images.

The ability to perform measurements over the extended measurement intervals required to observe small flow velocities is a unique capability compared to many of the flow-tagging velocimetry techniques that have been developed primarily for the study of high-speed flows, a non-exhaustive selection of which are introduced here in brief. Hiller et al. (1984) reported laser-induced phosphorescence of biacetyl for velocimetry; relatively long radiative lifetimes of the phosphorescent transition allowed camera delay times of up to 6 ms, sufficient for measuring $\mathcal{O}(1 \text{ m/s})$ velocities, but required an oxygen-free environment. Hassa and Hanson (1985) demonstrated laser-induced sulfur aerosols generated

by the photochemical decomposition of sulfur hexafluoride as an early alternative to smoke wires for seeding flows for Mie scattering visualization. Acetone molecular tagging velocimetry (MTV) was reported by Lempert et al. (2002) to exhibit maximum emission lifetimes of only 200 ns at extremely low, millibar pressures. By tagging a flow through the photodissociation of NO₂ and subsequently applying NO PLIF to interrogate the position of the dissociation products, which served as persistent chemical tags, Jiang et al. (2010) demonstrated MTV over longer timescales but at the expense of requiring a specialized pulse-burst laser and optical parametric oscillator. Krypton tagging velocimetry (KTV), as reported by Parziale et al. (2015), utilizes chemical tags in the form of metastable, excited-state krypton atoms with lifetimes on the order of 10 µs. KTV beneficially makes use of a chemically inert tracer, making it attractive for use in reactive environments, but brings with it a high cost for krypton seeding and the requirement of specialized dye lasers. In the femtosecond laser electronic excitation tagging (FLEET) technique, a seedless velocimetry method in which nitrogen molecules in air are tagged, Michael et al. (2011) report emission levels sufficient for the determination of the tagged position that are evident up to 30 µs after the laser pulse, providing the upper limit for the measurement interval.

FIV also shares some relation to image correlation velocimetry (ICV) methods first reported by Tokumaru and Dimotakis (1995) and since employed in various forms for seedless velocity measurements. ICV techniques use the correlation of successive images of features naturally present within a flow field to determine the magnitudes and direction of fluid motions and have been demonstrated utilizing numerous image types including Rayleigh scattering (Komiyama et al. 1996) and laser-induced fluorescence (Fielding et al. 2001) applied to turbulent flames, shadowgraphs of sprays (Sedarsky et al. 2013), and schlieren images (Jonassen et al. 2006). While these methods are attractive in many circumstances where inherent flow features can be tracked, ICV methods are not well suited to the core gas of region-5 shock-tube environment, where no such features naturally exist.

3 Experimental methods

The basic instrumentation requirements to perform 3-D FIV are an ignition source for a flame, and two perpendicularly arranged cameras from which the three velocity components can be extracted. In Sect. 3.1, such an experimental arrangement is described that builds upon the configuration of Ferris et al. (2019), with the critical addition of a sidewall camera to measure the axial components of the velocity. From the resulting images, velocities are extracted from



37 Page 4 of 16 Experiments in Fluids (2022) 63:37

flame centroid locations, following a procedure detailed in Sect. 3.2. Section 3.3 then describes a methodology for using measured incident and reflected shock velocities to calculate the region-5 state at locations in the shock tube other than the driven end wall.

3.1 Experimental setup

Experiments were performed in a stainless-steel, 11.5-cm-diameter shock tube, a facility described in detail by Campbell et al. (2014) and depicted in cross-section along with the associated instrumentation in Fig. 1. For the static characterization experiments reported in Sec. 4.1, the shock tube's sliding gate valve was closed, isolating the 40 cm of the tube nearest the driven end wall as a constant-volume, ambient-temperature, static vessel. Post-reflected-shock experiments were performed with the gate valve open and using conventional filling.

Figure 1 additionally shows the coordinate system as defined in this study. The Z direction is defined along the axis of the shock tube, with the positive direction defined as moving into the tube, away from the end wall; this is the horizontal direction in side-wall images. The X and Y axes are oriented radially within the shock tube, where Y is defined as the vertical axis visible in both the side- and end-wall views, and X is the horizontal direction viewed from the end wall.

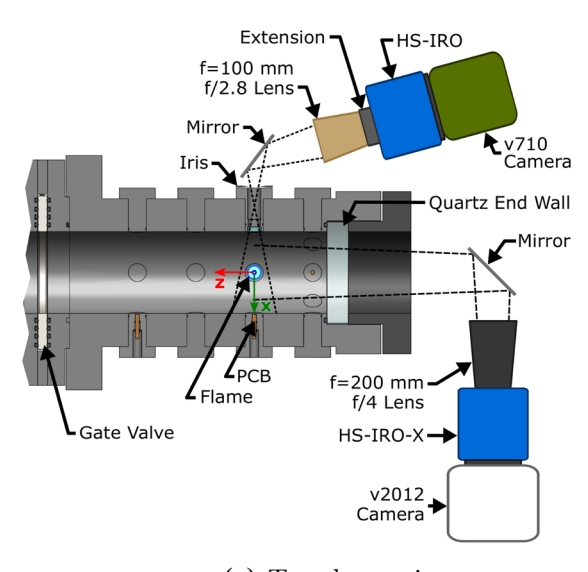
A Kistler pressure transducer located 2 cm from the driven end wall provides high-speed pressure measurements throughout the experiment. Fast-response pressure transducers (PCB Piezoelectronics) at four locations along the length of the tube record the step changes in pressure associated with the passage of the shock waves. All pressure signals were recorded at 10 MHz by a National Instruments

PXI-6115 multifunction data acquisition system; by logging the complete time-resolved pressure traces, the timing and speeds of both the incident and reflected shocks can be obtained from the PCB transducer data (Sect. 3.3).

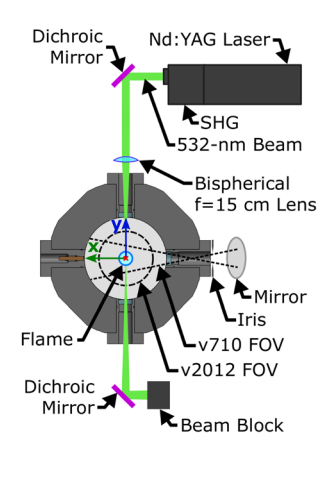
As in the shock-tube flame speed method, flames are ignited behind reflected shock waves 10.3 cm from the driven end wall by a plasma spark generated through LIB (Fig. 1). This method provides a physically non-intrusive means of igniting flames, an important consideration when post-incident-shock gas velocities of up to 1 km/s preclude the use of protruding electrodes. The 10.3-cm location is the optical port location second nearest the end wall in the shock-tube test section used in this work (Campbell et al. 2014) and that used in the majority of prior shock-tube flame studies (e.g., Ferris et al. 2019). A Q-switched, neodymium-doped yttrium aluminum garnet (Nd:YAG) laser (Solo PIV 120, New Wave Research) serves as the ignition-laser source. An integrated second-harmonic generation (SHG) cavity produces 532-nm light from the 1064-nm Nd:YAG output; the laser produces quoted pulse lengths of 3-5 ns and maximum pulse energies of 120 mJ at 532 nm. In practice, the pulse energy is reduced by shortening the O-switch delay time relative to the flash lamp from its optimal value $(\approx 180 \,\mu s)$. The spark timing after the reflected-shock passage (t_{snark}) is controlled through external triggering of the laser by an upstream PCB pressure transducer. The beam is focused by a 15-cm-focal-length, best-form bispherical lens to a focused beam waist (estimated waist diameter $\sim 10 \, \mu m$ based on manufacturer beam-quality specifications) at the center of the tube; it is at the beam waist where LIB occurs, creating a plasma spark that ignites an expanding flame.

A dual-camera imaging configuration was devised to provide simultaneous side-wall and end-wall imaging of flames in the shock tube, as represented in Fig. 1. A quartz

Fig. 1 Schematics of the instrumentation used in this work for a high-speed imaging and b igniting the flame. The cameras and ignition laser are out of plane in views (b) and (a), respectively, and are not shown for clarity. Camera ray tracing is approximate. Coordinate axes used in this work are shown centered on the flame in both views



(a) Top-down view



(b) Axial view



end-wall window provides axial optical access to the shock tube (Troutman et al. 2016). End-wall emission images were recorded by a Phantom v2012 camera (Vision Research) with an ultraviolet- (UV-) sensitive, high-speed intensified relay optic (HS-IRO-X, LaVision) outfitted with a 200-mm Nikkor lens. A 896- by 800-pixel sensor region was recorded at 20,000 frames per second (fps), a sufficiently large portion of the full-frame sensor to capture the complete 25-mm image circle of the HS-IRO-X. With this arrangement, a 7.2-cm FOV could be imaged at a spatial resolution of 123.6 pix/cm.

The limited side-wall optical access provided by a 1.8-cm-diameter port presented a unique imaging challenge. In order to maximize the FOV at the object plane, a large, f/2.8-aperture lens (Sodern Cerco) was used, offset by a 13-mm extension ring to produce a converging, hypercentric arrangement. An iris was positioned just outside the optical plug to restrict the collection angle of light, which helped to homogenize the spatial intensity profile observed at the object plane within the shock tube. With this arrangement, and the intensification provided by a HS-IRO (LaVision) to compensate for the low collection efficiency of emitted light, a roughly 2.5-cm FOV was imaged through the sidewall port using a reduced, 528- by 520-pixel sensor region of a Phantom v710 camera (Vision Research) at 191 pixelper-cm resolution and 20,000 fps. The collection of frames was synchronized to coincide with those of the end-wall recordings.

3.2 Velocimetry data interpretation

The process for extracting the bulk motion of flames from the emission videos, the heart of the FIV method, is described as follows and visually represented in Fig. 2. Emission images are binarized using a hysteresis thresholding method (Canny

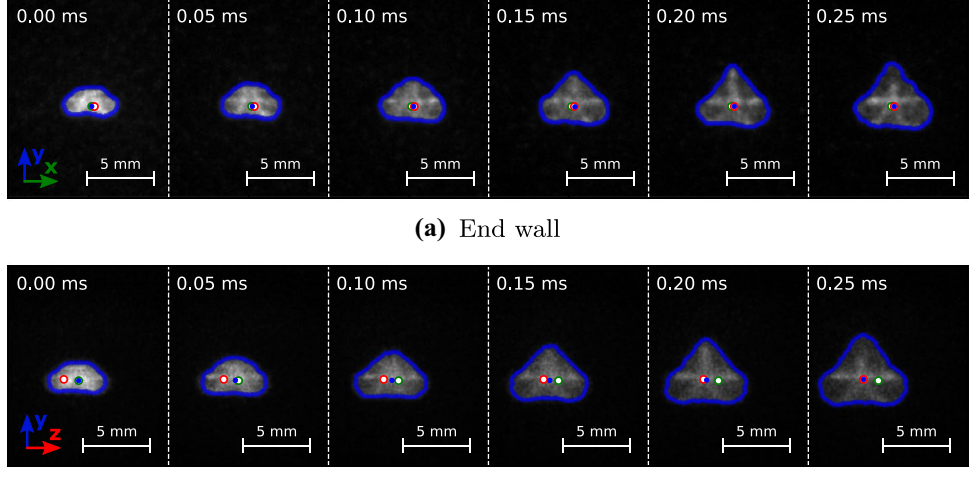
1986), with the upper and lower thresholds being chosen from among single and dual-level Otsu thresholds (Otsu 1979; Liao et al. 2001) such that the binary regions may be judged to subjectively coincide with the flames observed in each experiment. Binary images are cleaned using morphological closing and filling operations using open-source image processing tools available in Python through the SciPy (Virtanen and et al. 2020) and scikit-image (van der Walt et al. 2014) packages; borders of the resulting binary regions are shown as blue lines in Fig. 2. The centroids of the binary regions representing the flame are then extracted (solid blue dots in Fig. 2); end-wall images (Fig. 2a) provide X and Y positions, and side-wall images (Fig. 2b) provide Y and Z locations (see Fig. 1 for coordinate definition). Labeled times are relative to the first video frame following the spark.

The average velocity over the measurement interval is taken as the slope of a linear fit applied to the centroid-displacement vs. time data. Figure 3 shows examples of such fits obtained for the first six frames following the spark, spanning a measurement period of 250 μ s in a post-reflected-shock experiment. This same measurement interval was typical for measurements reported in this work, though a few experiments required the use of shorter, 150 μ s intervals. The velocity uncertainty of the fit, $\sigma_{u,fit}$, is taken as the range of slopes covered by the 95% confidence interval, which is calculated with an appropriate t-value to account for the small number of samples (Student 1908) and depicted as a shaded region accompanying each best-fit line in Fig. 3.

3.3 Thermodynamic state calculation

In order to calculate the thermodynamic state of the gas at the axial measurement location ($z_5 = 10.3$ cm) where the flame is ignited, a particle tracking argument is used to determine

Fig. 2 Representations of the image processing method applied to extract flame motions for a lean ($\phi = 0.5$) *n*-heptane/ O_2 /Ar experiment with $T_5 = 729$ K and $P_5 = 1.1$ atm (#17 in Table 3). Raw emission images are shown overlaid with blue borders of the flame regions identified through binarization; a solid blue marker identifies the location of the centroid in each image. The initial and final centroid locations are shown as open green and red circles, respectively, for reference of the flame's motion throughout the measurement period



(b) Side wall



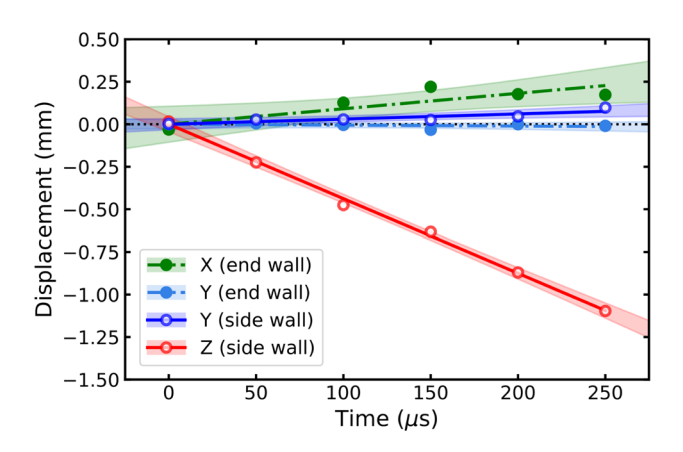


Fig. 3 Flame-drift displacements and linear velocity fits from the same n-heptane/O₂/Ar experiment shown in Fig. 2 (#17: $\phi = 0.5$, $T_5 = 729$ K, $P_5 = 1.1$ atm). Colors distinguish coordinate directions; line and marker styles identify the imaging perspective from which measurements were obtained

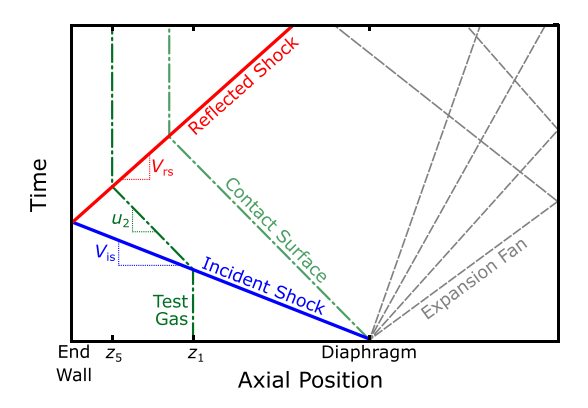
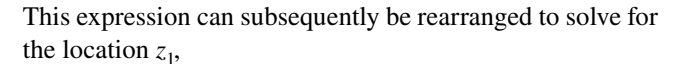


Fig. 4 Representative position-time (z-t) diagram of a shock-tube experiment illustrating the setup of the particle-tracking problem. The incident and reflected shocks are shown as solid blue and red lines, respectively. The path of the test gas first shocked at z_1 and reshocked at z_5 is shown as a dashed dark-green line

the position, z_1 , at which the gas is accelerated by the incident shock. The basic setup of this problem is shown in Fig. 4, where the left axis represents the driven-side end wall of the shock tube. Using the first-order approximation of constant lab-frame incident and shock velocities ($V_{\rm is}$ and $V_{\rm rs}$, respectively), the following expression is derived by equating the time needed for the region-2 gas to travel from z_1 to z_5 at velocity u_2 to the time required for the incident shock to reach the end wall at z=0, and subsequently reflect to reach z_5 ,

$$\frac{z_5 - z_1}{u_2} = \frac{0 - z_1}{V_{is}} + \frac{z_5 - 0}{V_{rs}}$$

$$\frac{z_5 - z_1}{u_2} = \frac{z_5}{V_{rs}} - \frac{z_1}{V_{is}}$$
(1)



$$z_1 = z_5 \left(\frac{u_2 - V_{\rm rs}}{u_2 - V_{\rm is}} \right) \left(\frac{V_{\rm is}}{V_{\rm rs}} \right) \tag{2}$$

All values required to solve for z_1 in Eq. 1 are either known, as is the case for z_5 , or can be evaluated from experimentally measurable quantities. By logging the pressure-time histories measured by the PCB pressure transducers, the timing of both the incident and reflected shocks can be detected, as illustrated in Fig. 5a. It is noted here that such reflected-shock velocity measurements would not be possible with the more conventional strategy of using differential timers to measure the incident shock velocity and subsequently calculating the reflected-shock velocity using normal shock jump relations, as with the FROSH code described by Campbell et al. (2017). With the locations of the PCB transducers precisely known, the velocities of the incident and reflected shocks are determined as a function of position by applying a linear fit to the differential velocities (Fig. 5b,c respectively for the incident and reflected shocks).

As previously mentioned, the impermeable boundary ensures that the region-5 gas is completely stagnated at the end wall. In order for this condition to be enforced, an additional constraint is imposed on the fit of the measured reflected shock velocities, wherein the end-wall (0-cm) value of the fit is fixed as $V_{rs,FROSH}$, the velocity determined by FROSH as necessary to stagnate the flow at the driven end wall. FROSH solves the normal shock jump equations assuming the mixture is chemically frozen but accounting for effects of vibrational relaxation. The thermodynamic assumption of full vibrational relaxation in both regions 2 and 5 is used in this work, as is appropriate for mixtures consisting of relatively high concentrations of hydrocarbon fuels (Campbell et al. 2017). The constrained reflectedshock fit, shown as the dash-dot line in Fig. 5c, is found to fall within the shaded confidence interval of the nominal, unconstrained fit (solid line). For the shock experiments reported in Sect. 4.2, the mean absolute difference between the intercept of the nominal best fits and $V_{rs,FROSH}$ was 3.6 m/s, about 1% of the observed values V_{rs} . The final parameter, u_2 , required to calculate z_1 using Eq. 2 is obtained using the normal-shock relations as the lab-frame gas velocity behind the incident shock of measured velocity V_{is} .

To accurately account for the change in shock velocity with position, V_{is} and u_2 should be evaluated at $z_{is} = z_1$ and V_{rs} at $z_{rs} = z_5$ when solving for z_1 . As such, a recursive solution method is appropriate, in which z_1^i at each iteration i is solved using Eq. 2 with V_{is} and u_2 evaluated using the previous solution z_1^{i-1} . Table 1 presents the key results of such a solution applied to the experiment shown in Fig. 5. The "end"



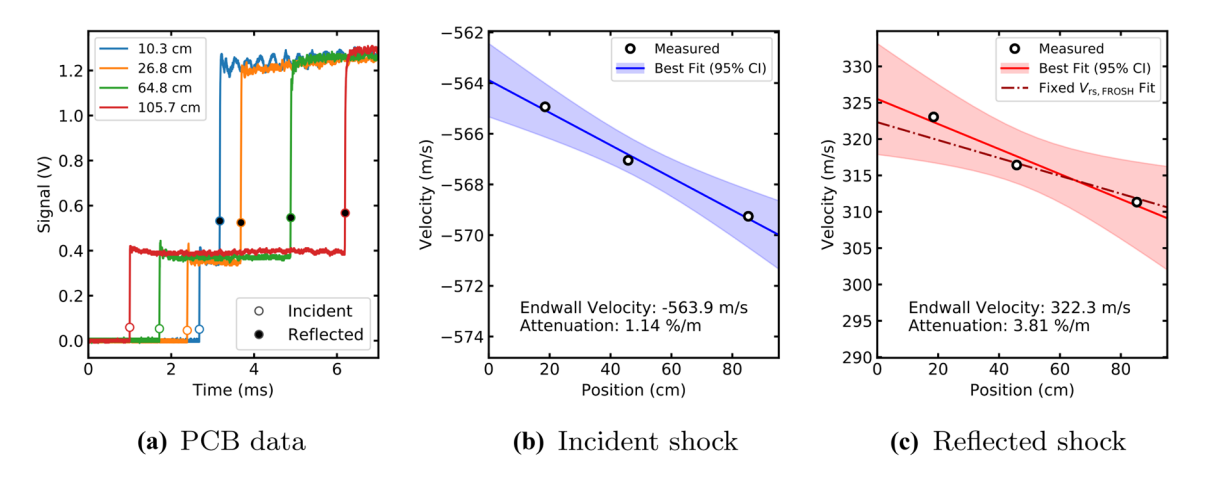


Fig. 5 Example shock-experiment data showing **a** identification of incident and reflected shocks from PCB data, **b** measured shock velocities and fit of incident-shock speed, and **c** fit of reflected-shock velocity measurements, showing the nominal best-fit line and the fit

with the end-wall $V_{\rm rs}$ value fixed. Confidence intervals (CI) are shown as shaded regions at the 95% level. Initial conditions: $T_1 = 294.6$ K, $P_1 = 75.6$ torr, composition: 0.0095 n-C₇H₁₆, 0.2081 O₂, 0.7824 Ar

Table 1 z_1 calculation parameters and results

Method:	End	Recursive		
	Wall	1 Step	Full	
z_{is} (cm)	0.0	45.92	46.51	
V_{is} (m/s)	-563.9	-566.8	-566.9	
u ₂ (m/s)	-314.1	-317.2	-317.3	
$z_{\rm rs}$ (cm)	0.0	10.3	10.3	
$V_{\rm rs}$ (m/s)	322.3	321.1	321.1	
<i>u</i> ₅ (m/s)	0.0	-1.99	-1.99	
z ₁ (cm)	45.92	46.50	46.51	

wall" column represents values evaluated at the driven end wall ($z_{\rm is}=z_{\rm rs}=0$), wherein the solved value of $z_{\rm 1}$ is taken as $z_{\rm 1}^0=z_{\rm is}$ to initialize the recursive solution method. The two columns under the "recursive" heading display results of the first recursive solution step and the fully converged solution; only negligible differences are found between the first and final solutions.

Additionally reported in Table 1 is the lab-frame, post-reflected-shock gas velocity, u_5 , calculated with FROSH by applying the normal shock relations using measured shock velocities and the constrained reflected-shock fit. The end-wall result of $u_5 = 0$ m/s reflects the boundary condition. At the 10.3-cm measurement location, a non-zero solution of $u_{5,\text{FROSH}} = -2.57$ m/s is found, indicating that the reflected shock is not sufficiently strong to fully stagnate the region-2 gas at locations offset from the end wall. This "residual velocity," $u_{5,\text{res}} = u_{5,\text{FROSH}}$, that remains after the reflected shock will be considered in Sect. 5.1 as one mechanism to account for the core-gas velocity measured using FIV in shock-tube experiments.

4 Results

4.1 Static characterization

Static flame experiments provide an opportunity to quantify the performance of the FIV method under known, zero-velocity conditions. Here, the results of eight static experiments are reported. All experiments were performed at ambient temperature ($T \approx 296 \text{ K}$) and pressures spanning from sub- to above-atmospheric ($P \in \{0.5, 1.0, 2.0\}$ atm). The oxidizer used in the fuel—air mixtures consisted of 21% oxygen (O₂) and 79% helium (He). Ethane (C₂H₆) was used as the fuel for the static experiments at unity equivalence ratio ($\phi = 1.0$).

The velocities measured in static experiments are shown graphically in Fig. 6 and summarized in Table 2. Considering first the X and Z velocity components, both the distribution of discrete measurements reflected in the plot and the summary statistics reported in the table show that, on average, the X and Z velocities capture the expected, static condition of the unburned gas. The mean values of the X and Z velocity measurements, -0.02 m/s and -0.13 m/s, are both near zero and well within the average measurement uncertainties ($\bar{\sigma}_{u,fit}$) of 0.35 m/s and 0.26 m/s, respectively. Furthermore, the close agreement between the standard deviations (std. dev.) and average uncertainties suggest that the spreads observed in the X and Z measurements are largely explained by the uncertainties of the centroid-position vs. time fits.

Unlike those in the other directions, the *Y*-component velocities show a systematic variation from the expected zero-velocity result. In Fig. 6, almost every discrete *Y*-velocity measurement falls more than its uncertainty from zero.



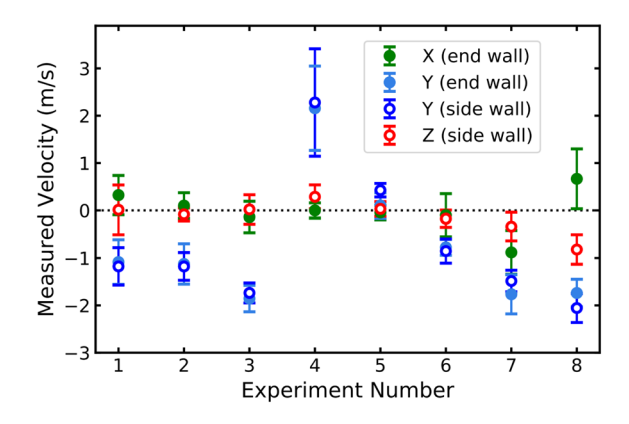


Fig. 6 Measured 3-D velocity components from 8 static experiments. Error bars show measurement uncertainty as the 95% confidence interval of the centroid-position vs. time fits. Colors correspond to the axes shown in Fig. 1

Table 2 Static experiment velocity statistics

Perspective	Axis	Mean (m/s)	Std. Dev. (m/s)	$\bar{\sigma}_{u,fit}$ (m/s)
End Wall	X	-0.02	0.41	0.35
	Y	-0.85	1.06	0.38
Side Wall	Y	-0.82	1.12	0.32
	Z	-0.13	0.31	0.26

These deviations manifest both as a systematic offset in the mean velocities and a random component in the standard deviations of the Y-axis measurements, both of which exceed the mean uncertainties, $\bar{\sigma}_{u.fit}$.

The duplicated measurement of the *Y*-axis velocity presents an opportunity to evaluate the self consistency of the FIV method and repeatability of the non-zero *Y*-direction results. Despite the variance from zero, the *Y*-axis velocities show a high degree of correlation (Fig. 7). Across all experiments, the two Y-velocity measurements are found to be within their joint uncertainty of one another, and the regression line of the measurements falls well within its confidence interval (CI) of the dotted reference line; both of these observations indicate the measurements are repeatable and that scatter observed in the *Y* velocities is not a result of random measurement error.

The relatively large variation in the Y-velocity measurements stems from the co-alignment of the Y axis with the path of the Nd:YAG laser used to ignite the flames. It has been widely reported that plasma kernels formed through laser-induced breakdown, along with subsequently ignited flame kernels, exhibit asymmetric growth along the axis of the laser (e.g., Phuoc 2006; Mulla et al. 2016). Dumitrache and Yalin (2020) attribute this asymmetric structure to

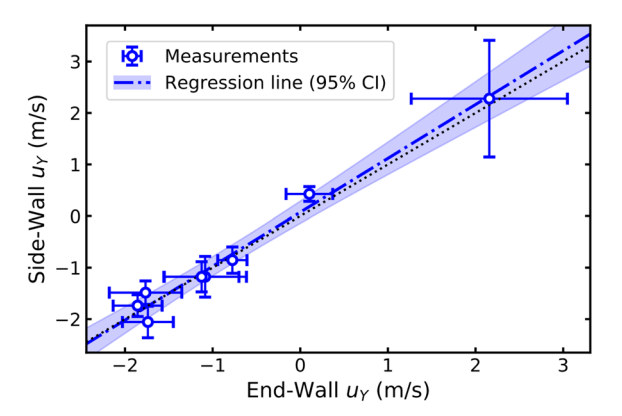


Fig. 7 Comparison of the *Y*-velocity components (along the ignition laser axis) measured in 8 static experiments. All measurements are found to be within their joint uncertainty of the dotted line (unity slope), indicating consistency between the side- and end-wall measurements

vorticity generated by the breakdown process that yields a toroidal ring propagating in the direction of travel of the igniting beam and a "third lobe" propagating backward toward the focusing lens. While the presence of these counter-propagating structures, and the flame morphology they induce, led to variability in the *Y* velocity components, the *X*- and *Z*-direction measurements, the latter of which is of primary interest in the post-reflected-shock measurements reported in the section that follows, are unaffected by this phenomenon.

4.2 Post-reflected-shock measurements

As an application of the FIV technique, measurements of the 3-D core gas velocity were performed behind reflected shock waves in 21 experiments covering a range of conditions detailed in Table 3. Propane (C_3H_8) and *n*-heptane (n-C₇H₁₆) were used as fuels, prepared at lean equivalence ratios (0.3 $\leq \phi \leq$ 0.9) with oxidizer mixtures consisting of 18.1% to 21.4% O2 balanced with various combinations nitrogen (N_2) , argon (Ar), and He to comprise the diluent(s). Post-reflected-shock temperatures computed following the methodology of Sect. 3.3 at the 10.3-cm measurement plane fell in the range 571 K $\leq T_5 \leq$ 1076 K and pressures varied from near atmospheric to elevated (1.03 atm $\leq P_5 \leq 1.88$ atm). Relatively short spark delay times (the time at which the flame is ignited following the reflected shock) in the range 0.3 ms $\leq t_{\text{spark}} \leq$ 2.5 ms were used for the reported measurements, defining the starting time of the 250 µs (typical) measurement interval.

The measured velocities are presented in Fig. 8, plotted against the post-reflected-shock temperature, T_5 . Each shock experiment provides four discrete velocity measurements: X and Y components from the end wall and Y and Z



#	T_5	P_5	Fuel	φ	Oxidizer			t _{spark}	
	(K)	(atm)		(-)	$\overline{\mathrm{O}_2}$	N_2	Ar	Не	(ms)
1	615	1.08	C_3H_8	0.8	0.19	_	0.39	0.42	1.26
2	613	1.07	C_3H_8	0.8	0.19	_	0.39	0.42	0.53
3	696	1.10	C_3H_8	0.8	0.19	_	0.39	0.42	0.66
4	719	1.10	C_3H_8	0.8	0.19	_	0.39	0.42	0.70
5	751	1.13	C_3H_8	0.8	0.19	_	0.39	0.42	1.44
6	752	1.14	C_3H_8	0.8	0.19	_	0.39	0.42	1.44
7	805	1.13	C_3H_8	0.8	0.19	_	0.39	0.42	1.51
8	860	1.03	C_3H_8	0.8	0.19	_	0.39	0.42	1.57
9	908	1.21	C_3H_8	0.8	0.19	_	0.39	0.42	1.62
10	1076	1.23	C_3H_8	0.8	0.19	_	0.39	0.42	0.76
11	828	1.13	C_3H_8	0.8	0.19	_	0.39	0.42	0.49
12	820	1.10	C_3H_8	0.8	0.19	_	0.39	0.42	2.49
13	669	1.10	C_3H_8	0.8	0.19	_	0.39	0.42	2.46
14	718	1.88	n - C_7H_{16}	0.9	0.18	_	0.41	0.41	2.05
15	721	1.06	n - C_7H_{16}	0.5	0.21	_	0.79	_	0.37
16	732	1.09	n-C ₇ H ₁₆	0.5	0.21	_	0.79	_	0.36
17	729	1.10	n - C_7H_{16}	0.5	0.21	_	0.79	_	0.33
18	744	1.10	n - C_7 H_{16}	0.3	0.21	_	0.79	_	0.34
19	758	1.12	C_3H_8	0.3	0.21	_	0.79	_	0.99
20	571	1.12	C_3H_8	0.8	0.20	0.40	_	0.40	1.69
21	619	1.11	C_3H_8	0.8	0.20	0.40	_	0.40	1.00

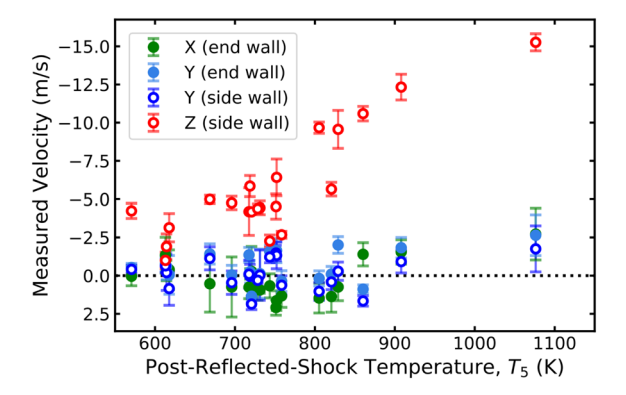


Fig. 8 Velocimetry results obtained from both the side- and end-wall perspectives during reflected-shock experiments. Error bars display the 95% confidence intervals of the velocity fits

components from the side wall. Statistics of the measurements, summarized across all shock experiments for each imaging perspective and coordinate axis, are provided in Table 4. Further details of the *Z*-axis velocity results are provided in the discussion section (Sect. 5.3, Table 5).

Across all the shock experiments, the X and Y components of the velocity were found to be small in magnitude (≤ 3 m/s) and show no clear trend with temperature. The mean, standard deviation, and average uncertainty of the X velocity measurements are all of larger magnitude than

Table 4 Shock experiment velocity statistics

Perspective	Axis	Mean (m/s)	Std. Dev. (m/s)	$\bar{\sigma}_{u,fit}$ (m/s)
End Wall	X	0.24	1.19	0.96
	Y	-0.66	1.00	0.66
Side Wall	Y	-0.11	0.98	0.72
	Z	-5.81	3.57	0.63

those recorded in static experiments, but still suggest that measurement accuracy of about 1 m/s is realizable using the FIV technique under practical conditions. The *Y* velocities show a systematic discrepancy of 0.55 m/s between the two perspectives, but remain correlated to a high degree (Fig. 9). At the higher temperatures in post-shock experiments, flames were found to form more pronounced third lobes in the direction of the laser. The systematic error between the measurements is believed to be a result of the side-wall imaging system having been more sensitive to the weak emission from this lobe, resulting in enhanced detection of the lobe during image binarization and leading to the positive bias seen in the *Y* velocities measured through the side-wall.

Unlike the randomly distributed *X* and *Y* velocities shown in Fig. 5, the *Z* velocity components tend to increase



37 Page 10 of 16 Experiments in Fluids (2022) 63:37

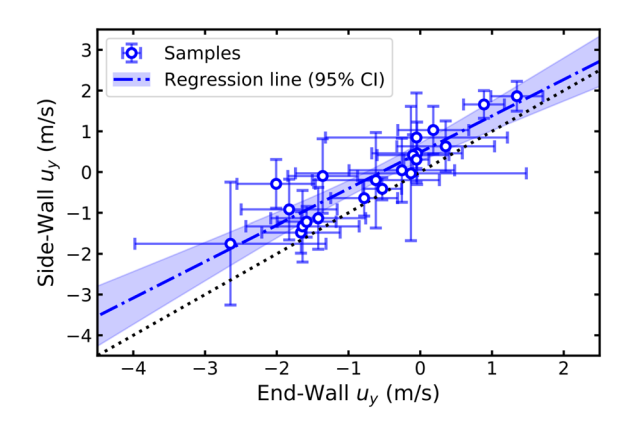


Fig. 9 Comparison of the *Y*-velocity components measured in the post-reflected-shock experiments, showing the correlation between the side- and end-wall measurements and slight positive bias of the side-wall

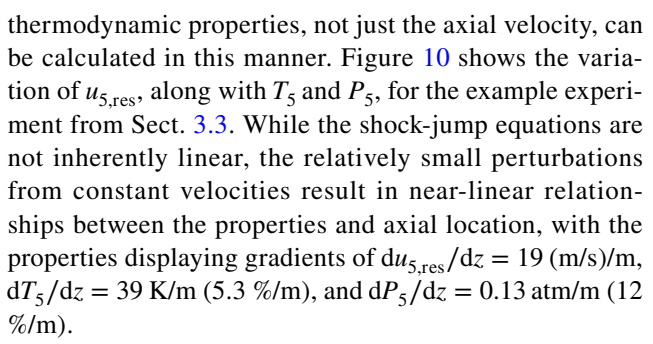
in magnitude with T_5 , conditions associated with stronger incident shocks and larger region-2 (post-incident-shock) gas velocities. The magnitudes of measured Z velocities, up to 10 m/s or greater, are significantly larger than the average measurement uncertainty ($\bar{\sigma}_{\rm u,fit}$). Furthermore, the negative bias of the mean velocity ($-5.83\,\rm m/s$) and fact that no single Z-velocity measurement was found to be positive provides strong evidence that the core gas in the shock-tube experiments does, in fact, retain a non-zero Z-axis velocity following its passage through the reflected shock, with the core-gas motion being directed toward the driven end wall of the tube. The nature of the Z velocity is the focus of the discussion that follows.

5 Discussion

This section discusses the finding of Z-axis velocity in the core gas of the shock tube following a reflected shock. As this section deals only with the Z component of the velocity field, the repeated specification of the velocity's direction is dropped for brevity. In the discussion that follows, $u_{5,\text{meas}}$ will refer to the measured, region-5 (post-reflected-shock), Z-axis velocities (corresponding to the red markers in Fig. 5). Details of the measured and modeled velocities discussed in this section are reported in Table 5 of Sect. 5.3.

5.1 Residual velocity

As established in the discussion of thermodynamic state calculation using measured values for $V_{\rm is}$ and $V_{\rm rs}$ (Sect. 3.3), the application of the shock-jump relations predict non-zero, negative values for the region-5 velocity at locations away from the end wall, termed the "residual velocity", $u_{\rm 5,res}$. In fact, axial variations in all the



The calculated $u_{5,res}$ values are presented in Fig. 11, with each data point plotted against the corresponding $u_{5,meas}$ to represent a single shock experiment and horizontal error bars displaying $\sigma_{u,fit}$. The calculated values $u_{5,res}$ agree reasonably well with $u_{5,meas}$ at relatively low velocities, however the agreement falls off for higher values $u_{5,meas}$. Therefore, while $u_{5,res}$ may be relevant to the

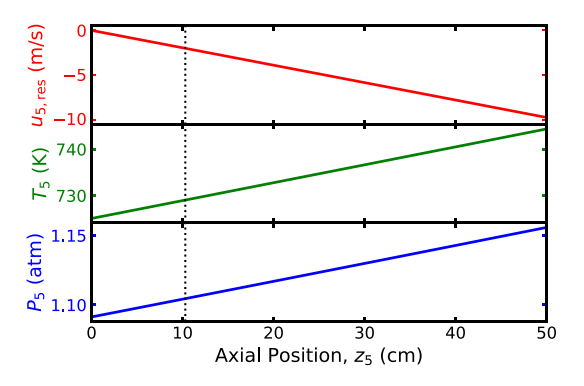


Fig. 10 Axial variation in the thermodynamic state $(u_5, T_5, \text{ and } P_5)$ of the region-5 gas calculated using measured $V_{\rm is}$ and $V_{\rm rs}$ for the experiment represented in Fig. 5 and Table 1. Vertical dotted line indicates the 10.3-cm measurement location used in this work

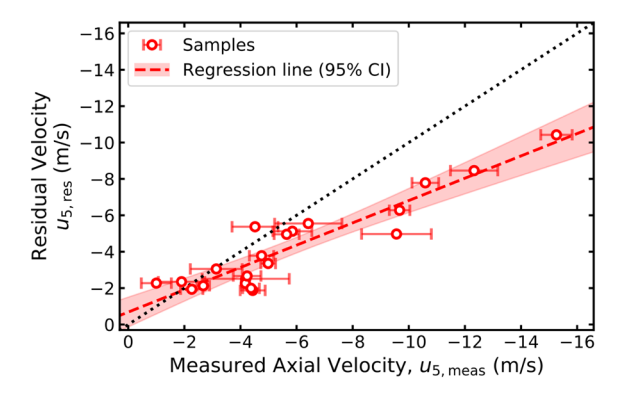


Fig. 11 Comparison of calculated residual velocity $u_{5,\text{res}}$ to observed velocity. Horizontal error bars represent measurement uncertainty. The dashed line is a best fit to the data, and the shaded region represents a 95% confidence interval of the fit. Dotted line of unity slope $(u_{5,\text{res}} = u_{5,\text{meas}})$ shown for reference



observed core-gas velocity, it cannot alone provide a satisfactory accounting for the measured results.

5.2 Pressure-change-induced velocity

As the residual velocity calculated from the shock-jump relations does not fully account for the observed velocity, the effect of variations in region-5 pressure, commonly referred to as dP/dt, is next considered. Post-reflected-shock pressure rise is an inherent result of boundary-layer effects and shock attenuation in shock-tube experiments, and numerous efforts have been reported to correlate (e.g., Petersen and Hanson 2001; Nativel et al. 2020), account for (e.g., Li et al. 2008; Hanson and Davidson 2014), and counteract (e.g., Hong et al. 2009; Grogan and Ihme 2020) the resulting impact. In this section, a model is proposed to use measured pressure data to predict an associated velocity within the core gas. The post-reflected-shock experiments are then evaluated using the new model, and the resulting calculated velocities are compared to those measured using FIV.

As a starting point for relating observed pressure changes to an axial velocity, it is convenient to consider the gas within the shock tube to be a cylinder of constant area, A, fixed at the driven end wall and undergoing isentropic compression (Fig. 12). Based on this simple, one-dimensional (1-D) model, an isentropic relation can be written between the cylinder length, L, and the pressure, P, relative to nominal values L_0 and P_0 :

$$\frac{P}{P_0} = \left(\frac{V_0}{V}\right)^{\gamma} = \left(\frac{A}{A}\frac{L_0}{L}\right)^{\gamma} = \left(\frac{L_0}{L}\right)^{\gamma}.$$
 (3)

Rearranging and differentiating Eq. 3 with respect to time, an expression can be found for the differential rate of change of the length in terms of the change in pressure:

$$\frac{\mathrm{d}L}{\mathrm{d}t} = \frac{-L}{\gamma} \frac{\mathrm{d}\ln P}{\mathrm{d}t}.\tag{4}$$

Recognizing that the rate of change in the length (dL/dt) is equivalent to the average velocity at which gas at that

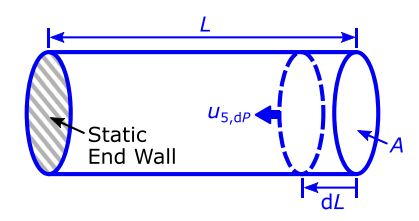


Fig. 12 Problem setup for deriving the velocity $u_{5,dP}$ of gas subjected to isentropic pressure change, posed as a quasi-1-D cylinder of gas with constant area A, and length L that changes as a result of moving the free interface on the right

location would have to move, the velocity associated pressure change, $u_{5 \text{ dP}}$, can then be defined as

$$u_{5,dP} \equiv \frac{-z_5}{\gamma} \frac{\mathrm{d} \ln P}{\mathrm{d}t},\tag{5}$$

where the substitution $L = z_5$ is made in order to evaluate the velocity at the measurement plane.

In order to make use of the model for $u_{5,\mathrm{dP}}$ defined in Eq. 5, the relative rate of pressure change, d ln $P/\mathrm{d}t$, must be evaluated from the recorded pressure data, a process illustrated in Fig. 13. Pressure data from the 2-cm Kistler pressure transducer are used, with the time the reflected shock passes the 10.3-cm measurement plane set equal to zero. The 10-MHz pressure measurements were first low-pass filtered with a 100-kHz cutoff frequency to remove high-frequency noise, then notch filtered using a filter of center frequency $f_{\rm c} = \frac{a_5}{2D} \frac{4}{\pi}$ corresponding to the frequency of a lateral pressure wave traveling at the speed of sound, a_5 , round trip across a tube of diameter, D, with the $\frac{4}{\pi}$ term as a geometric factor.

In order to extract meaningful rates $d \ln P/dt$ from the pressure data, additional noise reduction is required. Having already been low-pass filtered, the data are down-sampled to 500-kHz without incurring a loss of information. The down-sampled data are then processed with a local-polynomial filter (Savitzky and Golay 1964) of first order with a sampling window selected to match the 250 μ s measurement time of the FIV technique. The first derivative of the local polynomial fit is used to evaluate $d \ln P/dt$ (Fig. 13, bottom axis), thus avoiding the introduction of noise characteristic in discretely differentiated data. From the differential results, the nominal rate of $d \ln P/dt$ used to calculate $u_{5,dP}$ for a given experiment is taken as the average rate observed from time zero to the end of the FIV measurement window, and

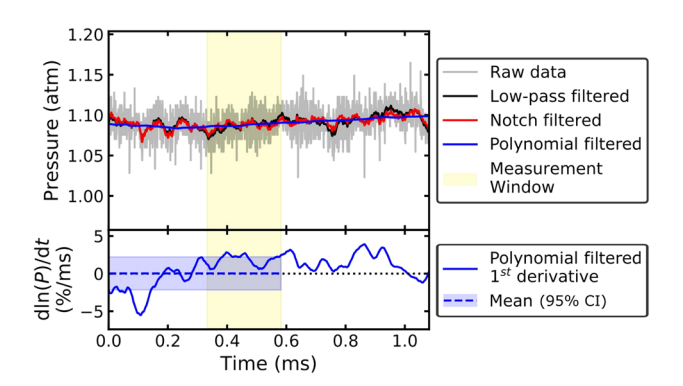


Fig. 13 Representative data processing applied to calculate the characteristic value of $d \ln P/dt$ for an experiment. The top axis displays the filtering of the raw pressure signal, while the bottom axis shows the extracted differential rate of change



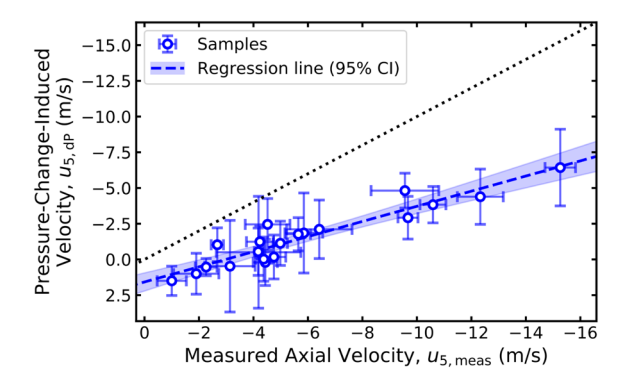


Fig. 14 Comparison of estimated $u_{5,dP}$ to observed velocity. Horizontal error bars represent measurement uncertainty; vertical error bars representative of the variation in the rate $d \ln P/dt$. The dashed line is a best fit to the data; the shaded region represents a 95% confidence interval of the fit. Dotted line of unity slope ($u_{5,dP} = u_{5,meas}$) shown for reference

the 95% confidence interval across this same time interval is taken as the uncertainty.

Calculated pressure-change-induced velocities, $u_{5,dP}$, are compared to experimentally measured $u_{5,meas}$ in Fig. 14. Across all experiments, the magnitudes of $u_{5,dP}$ are found to be insufficient to account for the observed axial velocity, even when the uncertainty of the rate of pressure change is taken into consideration. This observation importantly

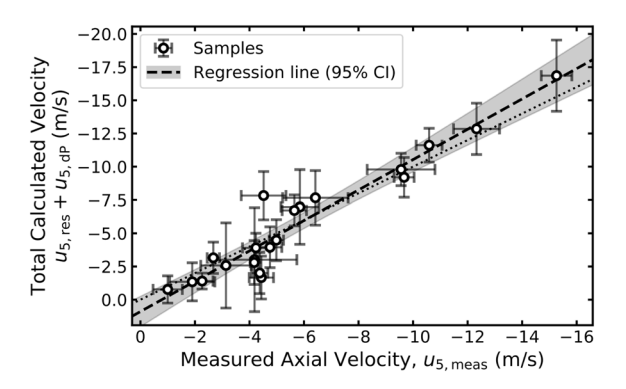


Fig. 15 Comparison of the combined residual and pressure-change-induced velocity to that measured using FIV. Velocities calculated using the combined model agree with those measured across all measurements within uncertainty, and the best-fit line of the results coincides nearly exactly with the dotted line of unity slope

demonstrates that higher-dimensional effects than those captured in this quasi-1-D pressure model are necessary to explain the observed velocity.

5.3 Combined velocity model

While neither of the two conceptual models, $u_{5,res}$ or $u_{5,dP}$, are able to independently account for the measured velocities,

Table 5 Shock experiment velocimetry results

#	<i>u</i> _{5,meas} (m/s)	<i>u</i> _{5,res} (m/s)	<i>u</i> _{5,dP} (m/s)	u _{5,total} (m/s)	$\Delta u_{5,(\text{meas-total})}$ (m/s)
1	-1.90 ± 0.83	-2.35	0.79 ± 1.45	-1.56 ± 1.45	-0.34 ± 1.67
2	-1.00 ± 0.54	-2.27	0.55 ± 1.25	-1.73 ± 1.25	0.73 ± 1.36
3	-4.75 ± 0.43	-3.78	-1.18 ± 1.73	-4.96 ± 1.73	0.20 ± 1.78
4	-5.85 ± 0.69	-5.12	-3.88 ± 2.47	-9.00 ± 2.47	3.15 ± 2.57
5	-4.52 ± 0.82	-5.37	-2.93 ± 1.05	-8.30 ± 1.05	3.78 ± 1.34
6	-6.42 ± 1.20	-5.55	-4.50 ± 0.72	-10.05 ± 0.72	3.63 ± 1.40
7	-9.67 ± 0.37	-6.28	-4.02 ± 1.46	-10.30 ± 1.46	0.63 ± 1.51
8	-10.59 ± 0.48	-7.79	-2.70 ± 2.10	-10.48 ± 2.10	-0.10 ± 2.16
9	-12.33 ± 0.84	-8.46	-3.50 ± 0.70	-11.96 ± 0.70	-0.37 ± 1.10
10	-15.26 ± 0.56	-10.42	-8.65 ± 2.79	-19.07 ± 2.79	3.81 ± 2.85
11	-9.56 ± 1.24	-4.97	-4.75 ± 2.32	-9.72 ± 2.32	0.16 ± 2.64
12	-5.65 ± 0.45	-4.96	-2.10 ± 0.85	-7.05 ± 0.85	1.41 ± 0.96
13	-4.99 ± 0.26	-3.36	-2.60 ± 1.87	-5.96 ± 1.87	0.97 ± 1.89
14	-4.19 ± 1.55	-2.51	-1.88 ± 4.77	-4.39 ± 4.77	0.21 ± 5.01
15	-4.17 ± 0.14	-2.26	-1.42 ± 2.58	-3.68 ± 2.58	-0.50 ± 2.58
16	-4.43 ± 0.45	-1.87	-0.68 ± 2.42	-2.56 ± 2.42	-1.88 ± 2.46
17	-4.38 ± 0.30	-1.99	-1.25 ± 1.03	-3.23 ± 1.03	-1.14 ± 1.07
18	-2.26 ± 0.40	-1.94	0.41 ± 1.31	-1.52 ± 1.31	-0.74 ± 1.37
19	-2.67 ± 0.22	-2.13	-0.84 ± 1.32	-2.97 ± 1.32	0.29 ± 1.34
20	-4.24 ± 0.49	-2.67	-2.01 ± 1.19	-4.67 ± 1.19	0.44 ± 1.29
21	-3.14 ± 0.93	-3.05	-2.67 ± 1.35	-5.72 ± 1.35	2.58 ± 1.64



the effect of combining the two models is finally considered. Figure 15 displays a comparison of the calculated total velocity $(u_{5,res} + u_{5,dP})$ compared to the measured velocities, and full details of the measured and modeled velocities are reported in Table 5, wherein experiment numbers refer to the experimental conditions reported in Table 3. The velocities are found to be in agreement across the wide variety of conditions covered by the experiments (571 K $\leq T_5 \leq 1,076$ K; 1.0 atm $\leq P_5 \leq$ 1.9 atm; various combinations of N₂, Ar, and He dilution), with nearly every calculated value falling within the joint uncertainty of the corresponding FIV measurement. Furthermore, the dotted reference line of unity slope falls within the confidence interval of the linear regression of the samples, demonstrating that the combined velocity model systematically captures the observed coregas velocities.

The use of a combined model, accounting independently for the effects of residual velocity resulting from shock attenuation and that induced by post-shock pressure change, can be rationalized if the two effects are thought of as exhibiting fundamentally different flow characteristics in the boundary region of the shock tube. Considering $u_{5,dP}$, it is apparent from the one-dimensional model in Fig. 12 that the velocity associated with pressure change must occur on an areaaveraged basis in order to produce the required volumetric change appearing in the starting form of the isentropic relation (Eq. 3). On the other hand, the shock-jump expressions used to calculate $u_{5,res}$ apply only in the core gas, without consideration of the flow in the boundary layers. If it is accepted that the boundary layer flow occurs in the opposite direction as the core flow, as was observed in the PIV experiments of Wagner et al. (2018), it could be imagined that the boundary-layer and core flows cancel one another on an area-averaged basis, producing no net flux through a given axial plane and, correspondingly, inducing no change in pressure. Under this assumption, the underlying flow fields would be separable, thus justifying the superposition utilized in the combined model. While this simple conceptual model neglects phenomena such as mass accumulation in a growing thermal boundary layer, the systematic accuracy of the combined-model results nonetheless suggest a level of utility provided by the ability to predict the core-gas velocity using only commonly used PCB and Kistler pressure measurements.

Examining the combined model's form allows several important features to be identified, with implications for the design and interpretation of shock-tube results. The 10.3-cm measurement location used in this work was much farther from the end wall than what is typical in conventional chemical kinetics or ignition experiments. Nevertheless, the functional forms of the two velocity components provide a mechanism by which these results can be generalized. Based on Fig. 10, $u_{5,\rm res}$ is expected to vary proportionally with the

axial position from the end wall. Similarly, Eq. 5 defining $u_{5 dP}$ includes a direct dependence with position z_5 . As such, a linear relationship between the total axial velocity and position can be expected, reaching a value of zero at the end wall. While the larger z_5 used here proved advantageous in that it magnified the velocity to a readily measurable level, the corresponding velocities at more typical measurement distances ($z_5 \le 2$ cm) could reasonably be assumed to be at least 5 times smaller than those measured here and likely negligible in the majority of 0-D kinetics experiments. Furthermore, through this linear dependence, it can be seen that velocities in the vicinity $3 \sim 7$ m/s at at a location 10 cm from the end wall in this work would be consistent, to a first-order approximation, with the PIV-measured velocities of order $40 \sim 100$ m/s at a location greater than 1 m from the end wall (Wagner et al. 2015, 2018).

Additionally, the dependence of $u_{5,res}$ on the shock attenuation rate, which is itself dependent on any number of factors that include features of the specific shock-tube facility and the experimental configuration (Petersen and Hanson 2001; Nativel et al. 2020), illustrates that many experimental design choices may affect the post-reflected-shock conditions. In cases where minimization of the axial velocity is important and cannot be achieved sufficiently by reducing the measurement distance, z_5 , attention must be directed to the shock attenuation rate and factors through which it can be reduced. The relevance of the attenuation rate also extends to the axial variations in other thermodynamic properties. For example, the axial temperature gradient could be relevant to the formation of remote ignition kernels associated with the onset of mild ignition events in ignition delay time measurements (Saytzev and Soloukhin 1961; Meyer and Oppenheim 1971; Hanson et al. 2013; Ninnemann et al. 2021). As such, reducing the shock attenuation rate might be expected to lessen the likelihood of mild ignition, though the recent simulation study of Kiverin et al. (2020) found longitudinal temperature variations to be a relatively small factor compared to other gas-dynamic effects in inducing mild ignition.

6 Conclusions and future work

Flame image velocimetry (FIV) was introduced as a seedless method capable of providing 3-D velocity measurements in flammable gas mixtures. The FIV method was first characterized in a static environment as a means to quantify the measurement uncertainty and accuracy. Velocity components measured in the X and Z directions were found to have average values near zero, and the average uncertainty of the fits (0.35 m/s and 0.26 m/s) and standard deviations (0.41 m/s and 0.31 m/s) indicate that the FIV method can provide velocity measurements with better than 1 m/s sensitivity and



37 Page 14 of 16 Experiments in Fluids (2022) 63:37

uncertainty. The *Y*-direction velocity components measured from the two perspectives were found to have similar average fit uncertainties (0.38 m/s and 0.32 m/s) but larger standard deviations (1.06 m/s and 1.12 m/s) and exhibited systematic average offsets from zero (-0.85 m/s and -0.82 m/s). The larger uncertainty in the *Y* direction is attributed to the local flow field induced by the LIB process.

Velocity measurements obtained in the core, region-5 gas were next obtained from reflected-shock experiments. Across all measurements, the uncertainties of the FIV fits were higher in the shocked experiments than those performed in a static environment, but still averaged less than 1 m/s in all component directions. In the two radial directions, X and Y, measured velocities were found to be randomly distributed with mean values near zero. In the Z direction aligned with the axis of the shock-tube, however, velocities larger in magnitude and negative in direction were observed, with magnitudes of up to 15 m/s being observed.

Three conceptual models, developed from experimentally measurable quantities, were evaluated based on their ability to explain the axial velocity in the core, region-5 gas. First, measured velocities of the incident and reflected shocks were used together with a particle-tracking argument to calculate axial variations in the thermodynamic state behind the reflected shock, including the residual velocity, $u_{5,res}$. Second, the relative rate of region-5 pressure change, $d \ln P/dt$, was used to calculate a corresponding velocity using a 1-D isentropic model. Finally, as neither model could independently account for the $u_{5,meas}$, a combined velocity model was proposed as the superposition of $u_{5,res}$ and $u_{5,dP}$. The combined model was found to produce calculated results that systematically agree with measured velocities. The direct dependence of the predicted axial velocity on position was found to reaffirm the quiescent-gas assumption when extrapolated to positions near the end wall and provides new insight into the parameters controlling the gas motion at larger distances relevant to the shock-tube flame speed method.

Opportunities to extend the FIV method demonstrated in this work exist through both extensions to analytical methods and newly enhanced diagnostic capabilities available to shock-tube studies. In a pair of recent studies, axial distortion was reported in flames ignited in the shock tube at elevated temperatures, suggesting the presence of more complex, three-dimensional flow fields within the region-5 gas under certain conditions (Susa and Hanson 2022; Susa et al. 2022). By combining laser-ignited flames with the ICV method applied over discrete segments of the flame surface and a physics-based flame propagation model, it may be possible to infer from the distortion that results the velocity field that would have had to have been present within the region-5 gas to explain it, as opposed to only the average, bulk velocity measured by the flame centroids

in the present work. Additionally, the ongoing deployment of shock tubes affording enhanced imaging access (e.g., Zabeti et al. 2017; Figueroa-Labastida and Farooq 2020; Ninnemann et al. 2021; Susa et al. 2022) are likely to benefit future FIV applications by providing additional experimental flexibility and enhanced data quality.

Acknowledgements This work was supported by the National Science Foundation under award number 1940865, contract monitor Dr. John Daily. Additional support was provided by the U.S. Army Research Laboratory and U.S. Army Research Office under contract/grant number W911NF-17-1-0420. A. J. Susa recognizes the U.S. Department of Defense for financial support through a NDSEG Fellowship. Additional thanks is provided to LaVision for providing the demonstration HS-IRO-X unit used in this work.

Author Contributions Both authors contributed to the study conception. A.J. Susa designed and performed the experiments, conducted the data analysis, developed the theoretical models, and prepared the first draft of the manuscript; R.K. Hanson provided resources and feedback throughout. Both authors contributed to manuscript revisions and approved the final manuscript.

Declarations

Conflict of Interest The authors have no conflicts of interest to declare that are relevant to the content of this article.

Publication History A partial, preliminary version of this study was presented at the 12th U.S. National Combustion Meeting, May 24-26, 2021 under the title "Flame-drift velocimetry and flame morphology measurements with dual-perspective imaging in a shock tube."

References

Bauer S (1963) Chemical kinetics in shock tubes. Science 141(3584):867–879. https://doi.org/10.1126/science.141.3584. 867

Beduneau J, Kawahara N, Nakayama T et al (2009) Laser-induced radical generation and evolution to a self-sustaining flame. Combust Flame 156(3):642–656. https://doi.org/10.1016/j.combustflame.2008.09.013

Berger L, Hesse R, Kleinheinz K et al (2020) A DNS study of the impact of gravity on spherically expanding laminar premixed flames. Combust Flame 216:412–425. https://doi.org/10.1016/j.combustflame.2020.01.036

Camm J, Davy M, Fang X, et al (2018) The Oxford cold driven shock tube (CDST) for fuel spray and chemical kinetics research. SAE Technical Papers pp Article: 2018–01–0222. https://doi.org/10.4271/2018-01-0222

Campbell MF, Tulgestke AM, Davidson DF et al (2014) A secondgeneration constrained reaction volume shock tube. Rev Sci Instrum 85(5):055,108. https://doi.org/10.1063/1.4875056

Campbell MF, Owen KG, Davidson DF et al (2017) Dependence of calculated postshock thermodynamic variables on vibrational equilibrium and input uncertainty. J Thermophys Heat Transfer 31(3):586–608. https://doi.org/10.2514/1.T4952

Canny J (1986) A computation approach to edge detection. IEEE Trans Pattern Anal Mach Intell 8(6):670–700. https://doi.org/10.1109/TPAMI.1986.4767851



- Davidson D, Hong Z, Pilla G et al (2010) Multi-species time-history measurements during n-heptane oxidation behind reflected shock waves. Combust Flame 157(10):1899–1905. https://doi.org/10.1016/j.combustflame.2010.01.004
- Davies L, Wilson J (1969) Influence of reflected shock and boundary-layer interaction on shock-tube flows. Phys Fluids 12(5):1–37. https://doi.org/10.1063/1.1706244
- Dumitrache C, Yalin AP (2020) Gas dynamics and vorticity generation in laser-induced breakdown of air. Opt Express 28(4):5835–5850. https://doi.org/10.1364/OE.385430
- Emanuel G (2000) Theory of shock waves. In: Ben-Dor G, Igra O, Elperin T (eds) Handbook of shock waves, vol 1. Elsevier, Amsterdam, pp 185–262
- Ferris AM, Susa AJ, Davidson DF et al (2019) High-temperature laminar flame speed measurements in a shock tube. Combust Flame 205:241–252. https://doi.org/10.1016/j.combustflame. 2019.04.007
- Fielding J, Long MB, Fielding G et al (2001) Systematic errors in optical-flow velocimetry for turbulent flows and flames. Appl Opt 40(6):757–764. https://doi.org/10.1364/AO.40.000757
- Figueroa-Labastida M, Farooq A (2020) Simultaneous lateral and endwall high-speed visualization of ignition in a circular shock tube. Combust Flame 214:263–265. https://doi.org/10.1016/j.combustflame.2019.12.033
- Gaydon AG, Hurle IR (1963) The shock tube in high-temperature chemical physics. Reinhold Publishing Corporation, New York
- Grogan K, Ihme M (2020) Stanshock: a gas-dynamic model for shock tube simulations with non-ideal effects and chemical kinetics. Shock Waves 30(4):425–438. https://doi.org/10.1007/ s00193-019-00935-x
- Grogan KP, Ihme M (2017) Regimes describing shock boundary layer interaction and ignition in shock tubes. Proc Combust Inst 36(2):2927–2935. https://doi.org/10.1016/j.proci.2016.06.078
- Hanson RK, Davidson DF (2014) Recent advances in laser absorption and shock tube methods for studies of combustion chemistry. Prog Energy Combust Sci 44:103–114. https://doi.org/10.1016/j.pecs.2014.05.001
- Hanson RK, Pang GA, Chakraborty S et al (2013) Constrained reaction volume approach for studying chemical kinetics behind reflected shock waves. Combust Flame 160(9):1550–1558. https://doi.org/10.1016/j.combustflame.2013.03.026
- Hassa C, Hanson R (1985) Fast laser-induced aerosol formation for visualization of gas flows. Rev Sci Instrum 56(4):557–559. https://doi.org/10.1063/1.1138286
- Hiller B, Booman R, Hassa C et al (1984) Velocity visualization in gas flows using laser-induced phosphorescence of biacetyl. Rev Sci Instrum 55(12):1964–1967. https://doi.org/10.1063/1. 1137687
- Hong Z, Pang GA, Vasu SS et al (2009) The use of driver inserts to reduce non-ideal pressure variations behind reflected shock waves. Shock Waves 19(2):113–123. https://doi.org/10.1007/s00193-009-0205-y
- Huang J, Hill P, Bushe W et al (2004) Shock-tube study of methane ignition under engine-relevant conditions: experiments and modeling. Combust Flame 136(1–2):25–42. https://doi.org/10.1016/j.combustflame.2003.09.002
- Jiang N, Nishihara M, Lempert WR (2010) Quantitative NO₂ molecular tagging velocimetry at 500 kHz frame rate. Appl Phys Lett 97(22):221,103. https://doi.org/10.1063/1.3522654
- Jo S, Gore JP (2022) Laser ignition energy for turbulent premixed hydrogen air jets. Combust Flame 236(111):767. https://doi.org/ 10.1016/j.combustflame.2021.111767
- Jonassen DR, Settles GS, Tronosky MD (2006) Schlieren "piv" for turbulent flows. Optics and Lasers in Engineering 44(3–4):190–207. https://doi.org/10.1016/j.optlaseng.2005.04.004

- Jones S, Thomas G, Ibrahim S (1998) A new experimental technique for the study of turbulent premixed flames. In: Symposium (International) on combustion, Elsevier, pp 935–940, https://doi.org/10. 1016/S0082-0784(98)80491-8
- Kiverin AD, Minaev KO, Yakovenko IS (2020) Modes of mild ignition in shock tubes: origins and classification. Combust Flame 221:420–428. https://doi.org/10.1016/j.combustflame.2020.08.013
- Kleine H, Lyakhov V, Gvozdeva L et al (1992) Bifurcation of a reflected shock wave in a shock tube. Shock Waves. https://doi.org/10.1007/978-3-642-77648-9 36
- Kobayashi Y, Tsujino T, Nakaya S et al (2019) Laser-induced spark ignition of DME-air mixtures in microgravity: comparison of ignition characteristics between normal gravity and microgravity. Fuel 236:1391–1399. https://doi.org/10.1016/j.fuel.2018.09.124
- Komiyama M, Miyafuji A, Takagi T (1996) Flamelet behavior in a turbulent diffusion flame measured by rayleigh scattering image velocimetry. In: Symposium (International) on combustion, Elsevier, pp 339–346, https://doi.org/10.1016/S0082-0784(96) 80234-7
- Lempert WR, Jiang N, Sethuram S et al (2002) Molecular tagging velocimetry measurements in supersonic microjets. AIAA J 40(6):1065–1070. https://doi.org/10.2514/2.1789
- Li H, Owens Z, Davidson D et al (2008) A simple reactive gasdynamic model for the computation of gas temperature and species concentrations behind reflected shock waves. Int J Chem Kinet 40(4):189–198. https://doi.org/10.1002/kin.20305
- Liao PS, Chen TS, Chung PC et al (2001) A fast algorithm for multi-level thresholding. J Inf Sci Eng 17(5):713–727. https://doi.org/10.6688/JISE.2001.17.5.1
- Mark H (1958) The interaction of a reflected shock wave with the boundary layer in a shock tube. National Advisory Committee for Aeronautics
- Melling A (1997) Tracer particles and seeding for particle image velocimetry. Meas Sci Technol 8(12):1406. https://doi.org/10. 1088/0957-0233/8/12/005
- Meyer J, Oppenheim A (1971) On the shock-induced ignition of explosive gases. In: Symposium (International) on combustion, Elsevier, pp 1153–1164, https://doi.org/10.1016/S0010-2180(72) 80183-4
- Michael JB, Edwards MR, Dogariu A et al (2011) Femtosecond laser electronic excitation tagging for quantitative velocity imaging in air. Appl Opt 50(26):5158–5162. https://doi.org/10.1364/AO.50.005158
- Mulla IA, Chakravarthy SR, Swaminathan N et al (2016) Evolution of flame-kernel in laser-induced spark ignited mixtures: a parametric study. Combust Flame 164:303–318. https://doi.org/10.1016/j. combustflame.2015.11.0290010-2180
- Nativel D, Cooper SP, Lipkowicz T et al (2020) Impact of shock-tube facility-dependent effects on incident-and reflected-shock conditions over a wide range of pressures and mach numbers. Combust Flame 217:200–211. https://doi.org/10.1016/j.combustflame. 2020.03.023
- Ninnemann E, Koroglu B, Pryor O et al (2018) New insights into the shock tube ignition of h2/o2 at low to moderate temperatures using high-speed end-wall imaging. Combust Flame 187:11–21. https://doi.org/10.1016/j.combustflame.2017.08.021
- Ninnemann E, Pryor O, Barak S et al (2021) Reflected shock-initiated ignition probed via simultaneous lateral and endwall high-speed imaging with a transparent, cylindrical test-section. Combust Flame 224:43–53. https://doi.org/10.1016/j.combustflame.2020. 08.017
- Otsu N (1979) A threshold selection method from gray-level histograms. IEEE Trans Syst Man Cybern 9(1):62–66. https://doi.org/10.1109/TSMC.1979.4310076



- Parziale N, Smith M, Marineau E (2015) Krypton tagging velocimetry of an underexpanded jet. Appl Opt 54(16):5094–5101. https://doi.org/10.1364/AO.54.005094
- Petersen EL, Hanson RK (2001) Nonideal effects behind reflected shock waves in a high-pressure shock tube. Shock Waves 10(6):405–420. https://doi.org/10.1007/PL00004051
- Phuoc TX (2006) Laser-induced spark ignition fundamental and applications. Opt Lasers Eng 44(5):351–397. https://doi.org/10.1016/j.optlaseng.2005.03.008
- Savitzky A, Golay MJ (1964) Smoothing and differentiation of data by simplified least squares procedures. Anal Chem 36(8):1627–1639. https://doi.org/10.1021/ac60214a047
- Saytzev S, Soloukhin R (1961) Study of combustion of an adiabatically-heated gas mixture. In: Symposium (International) on combustion, Elsevier, pp 344–347, https://doi.org/10.1016/S0082-0784(06)80522-9
- Sedarsky D, Idlahcen S, Rozé C et al (2013) Velocity measurements in the near field of a diesel fuel injector by ultrafast imagery. Exp Fluids 54(2):1–12. https://doi.org/10.1007/s00348-012-1451-9
- Shepherd W (1948) The ignition of gas mixtures by impulsive pressures. In: Symposium on combustion and flame, and explosion phenomena, Elsevier, pp 301–316, https://doi.org/10.1016/S1062-2896(49)80037-7
- Shi Z, Hardalupas Y, Taylor AM (2019) Laser-induced plasma image velocimetry. Exp Fluids 60(1):1–13. https://doi.org/10.1007/s00348-018-2649-2
- Student (1908) The probable error of a mean. Biometrika, 1–25. https://doi.org/10.2307/2331554
- Susa AJ, Hanson RK (2022) Distortion of expanding n-heptane flames at high unburned-gas temperatures behind reflected shocks. Combust Flame 237(111):842. https://doi.org/10.1016/j.combustflame. 2021.111842
- Susa AJ, Ferris AM, Davidson DF et al (2019) Experimental observation of negative temperature dependence in iso-octane burning velocities. AIAA J 57(10):4476–4481. https://doi.org/10.2514/1. J058530
- Susa AJ, Zheng L, Hanson RK (2021) Schlieren-based measurements of propane flame speeds at extreme temperatures. In: 12th US national combustion meeting, p 1G05
- Susa AJ, Zheng L, Nygaard ZD, et al (2022) End-wall effects on freely propagating flames in a shock tube. In: AIAA Scitech 2022 Forum

- Tokumaru P, Dimotakis P (1995) Image correlation velocimetry. Exp Fluids 19(1):1–15. https://doi.org/10.1007/BF00192228
- Troutman V, Strand C, Campbell M et al (2016) High-speed oh* chemiluminescence imaging of ignition through a shock tube end-wall. Appl Phys B 122(3):56. https://doi.org/10.1007/s00340-016-6326-y
- Tsang W, Lifshitz A (1990) Shock tube techniques in chemical kinetics. Annu Rev Phys Chem 41(1):559–599. https://doi.org/10.1146/annurev.pc.41.100190.003015
- van der Walt S, Schönberger JL, Nunez-Iglesias J et al (2014) scikitimage: image processing in Python. PeerJ 2:e453. https://doi.org/ 10.7717/peerj.453
- Virtanen P et al (2020) SciPy 1.0: fundamental algorithms for scientific computing in python. Nat Methods 17:261–272. https://doi.org/10.1038/s41592-019-0686-2
- Wagner J, Beresh SJ, DeMauro EP, et al (2015) Time-resolved PIV in a shock tube using a pulse-burst laser. In: 11th international symposium on particle image velocimetry
- Wagner JL, DeMauro EP, Casper KM et al (2018) Pulse-burst PIV of an impulsively started cylinder in a shock tube for Re > 10⁵. Exp Fluids 59(6):1–16. https://doi.org/10.1007/s00348-018-2558-4
- Weber YS, Oran E, Boris J et al (1995) The numerical simulation of shock bifurcation near the end wall of a shock tube. Phys Fluids 7(10):2475–2488. https://doi.org/10.1063/1.868691
- Willert C, Stockhausen G, Voges M, et al (2007) Selected applications of planar imaging velocimetry in combustion test facilities, Springer, pp 283–309. https://doi.org/10.1007/978-3-540-73528-1 15
- Yamashita H, Kasahara J, Sugiyama Y et al (2012) Visualization study of ignition modes behind bifurcated-reflected shock waves. Combust Flame 159(9):2954–2966. https://doi.org/10.1016/j.combustflame.2012.05.009
- Yoo J, Mitchell D, Davidson D et al (2010) Planar laser-induced fluorescence imaging in shock tube flows. Exp Fluids 49(4):751–759. https://doi.org/10.1007/s00348-010-0876-2
- Zabeti Š, Fikri M, Schulz C (2017) Reaction-time-resolved measurements of laser-induced fluorescence in a shock tube with a single laser pulse. Rev Sci Instrum 88(11):115,105. https://doi.org/10.1063/1.5010228

Publisher's Note Springer Nature remains neutral with regard to jurisdictional claims in published maps and institutional affiliations.

